J. Fluid Mech. (2021), *vol.* 912, R1, doi:10.1017/jfm.2020.1147

JFM RAPIDS

Water entry of spheres into a rotating liquid

Lei Yi[1], **Shuai Li**[2,3], **Hechuan Jiang**[1], **Detlef Lohse**[3,4], **Chao Sun**[1,5] **and Varghese Mathai**[6,†]

[1]Center for Combustion Energy, Key Laboratory for Thermal Science and Power Engineering of Ministry of Education, Department of Energy and Power Engineering, Tsinghua University, 100084 Beijing, PR China

[2]College of Shipbuilding Engineering, Harbin Engineering University, 150001 Harbin, PR China

[3]Physics of Fluids Group and Max Planck Center Twente, MESA+ Institute and J.M. Burgers Center for Fluid Dynamics, University of Twente, P.O. Box 217, 7500AE Enschede, The Netherlands

[4]Max Planck Institute for Dynamics and Self-Organization, 37077 Göttingen, Germany

[5]Department of Engineering Mechanics, School of Aerospace Engineering, Tsinghua University, Beijing 100084, PR China

[6]Department of Physics, University of Massachusetts, Amherst, MA 01003, USA

(Received 3 October 2020; revised 21 November 2020; accepted 13 December 2020)

The transient cavity dynamics during water entry of a heavy, non-rotating sphere impacting a rotating pool of liquid is studied experimentally, numerically and theoretically. We show that the pool rotation advances the transition of the cavity type – from deep seal to surface seal – marked by a reduction in the transitional Froude number. The role of the dimensionless rotational number $\mathcal{S} \equiv \omega R_0/U_0$ on the transient cavity dynamics is unveiled, where R_0 is the sphere radius, ω the angular speed of the liquid and U_0 the impact velocity. The rotating background liquid has two discernible effects on the cavity evolution. Firstly, an increase in the underwater pressure field due to centripetal effects; and secondly, a reduction in the pressure of airflow in the cavity neck near the water surface. The non-dimensional pinch-off time of the deep seal shows a robust $1/2$ power-law dependence on the Froude number, but with a reducing prefactor for increasing ω. Our findings reveal that the effects of a rotating background liquid on the water entry can be traced back to the subtle differences in the initial stage splash and the near-surface cavity dynamics.

Key words: flow–structure interactions

---

† Email address for correspondence: vmathai@umass.edu

1. Introduction

The impact of a solid body into water comprises a complex series of events that occur both above and below the water surface and depend on the configuration of the body. The phenomena of interest are the associated splash, the cavities and the jets (Prosperetti & Oguz 1993; Truscott, Epps & Belden 2014), which have wide relevance in fields ranging from water-skipping animals to air-to-sea projectiles and even to planetary crater formation (Lohse *et al.* 2004; Hu & Bush 2010; Van Der Meer 2017). The nature of the splash and its closure (initial-stage events) often have long-lasting implications for the underwater events that follow (Thoroddsen *et al.* 2004; Aristoff *et al.* 2010; Mansoor *et al.* 2014). An important factor that determines the characteristics of splash is the surface wettability (contact angle) of the impactor. For instance, increased wettability can induce an increase in the splash formation threshold (Duez *et al.* 2007), whereas a superhydrophobic surface coating can lead to the formation of a drag-reducing, underwater cavity during water entry (Vakarelski *et al.* 2017). The airflow rushing into this cavity also plays a significant role in the dynamics of the splash curtain that forms above the free surface (Thoroddsen *et al.* 2011; Vincent *et al.* 2018; Eshraghi, Jung & Vlachos 2020).

The dimensional parameters considered in prior studies are usually the density (or pressure) of the air above the water surface, the impact velocity, the projectile's shape and temperature, and the liquid properties (Enriquez *et al.* 2012; Truscott *et al.* 2014; Mathai, Govardhan & Arakeri 2015; Peters *et al.* 2016; Mansoor *et al.* 2017; Aly & Asai 2018; Zhang *et al.* 2018). Within this parameter space, a variety of splash and cavity types are possible, *viz.* the quasi-static seal, shallow seal, deep seal and surface seal. In the inertial regime (moderate to high-speed impact), the crucial parameter is the Froude number Fr, which determines the specific type of water entry (Aristoff & Bush 2009). Within the air-entraining regime of water entry (Truscott *et al.* 2014; Hao, Zhang & Huang 2018), the collapse of the subsurface cavity displays a non-universal, Froude-number-dependent power-law exponent (Bergmann *et al.* 2006) that approaches a 1/2 scaling in the limit of large Fr (Lohse *et al.* 2004; Duclaux *et al.* 2007; Bergmann *et al.* 2009*b*). Similarly, the pinch-off depth of the cavity displays two distinct scaling regimes with Froude number, separated by discrete jumps (Gekle *et al.* 2008).

A spinning projectile during water entry can produce several interesting features. For example, helical striations have been seen on the cavity surface during the water entry of a rotating projectile (Shi, Itoh & Takami 2000). Also, imparting a transverse spin to a water-entering projectile can cause the development of non-axisymmetric cavities. These show interesting similarities to the cavities formed by spheres with a half-hydrophilic and half-hydrophobic surface (Truscott & Techet 2009*b*,*a*). A modification to the problem presented above is achieved when a background rotational motion is provided to the pool prior to water entry. Although rotation in the carrier liquid has been found to have a profound influence on a variety of fluid dynamical phenomena (Alvarez-Lacalle, Casademunt & Eggers 2009; Bergmann *et al.* 2009*a*; Jiang *et al.* 2020; Mathai, Lohse & Sun 2020), its effect on the water entry of spheres has not been studied.

In the present work, we explore the familiar water entry phenomenon in the presence of background pool rotation, using experiments, numerical simulations and theoretical analysis. The liquid flow condition here essentially mimics the vortex core of a whirlpool (Stepanyants & Yeoh 2008), i.e. an azimuthal flow resembling a rigidly rotating liquid. We begin with a description of the experimental set-up and the numerical method. We reveal how the background liquid rotation alters both the splash and the cavity dynamics, triggering an earlier transition from deep seal to surface seal. Lastly, we provide scaling arguments to explain the observed cavity evolution and pinch-off dynamics.

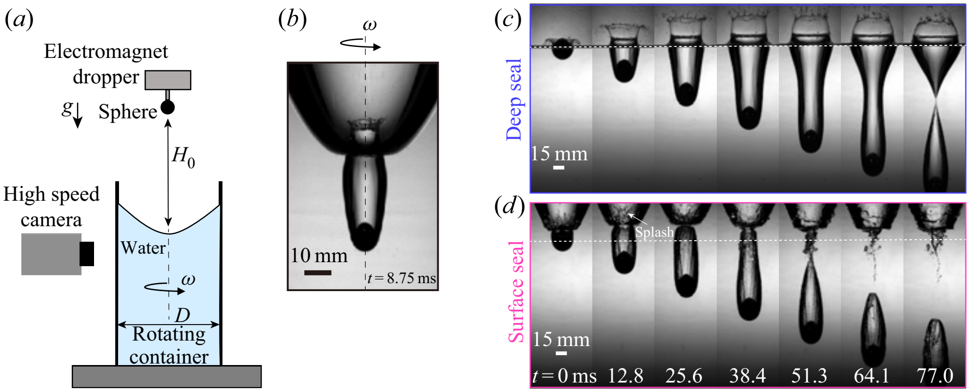

Figure 1. (*a*) Schematic diagram of the experimental set-up, wherein a steel sphere with radius R_0 is released from a height H_0 before impacting a rotating pool of water (angular velocity ω). (*b*) A representative image showing the underwater cavity formed by the sphere (radius $R_0 = 5$ mm) upon water entry at an impact velocity $U_0 = 2.86\ \mathrm{m\,s^{-1}}$ in a pool rotating at an angular velocity $\omega = 8\pi\ \mathrm{rad\,s^{-1}}$. Here, $Fr = 167$ and $\mathcal{S} = 0.044$. (*c*) Water entry sequence in the quiescent liquid case ($\mathcal{S} = 0$) with a deep seal type of cavity. The horizontal dashed line denotes the undisturbed free surface. (*d*) Water entry sequence in the rotating liquid case ($\omega = 8\pi\ \mathrm{rad\,s^{-1}}$, $\mathcal{S} = 0.16$) with a surface seal type of cavity. The horizontal dashed line again indicates the initial lowest position of the undisturbed free surface. The splash evolution here is not clearly discernible due to the parabolic free surface. For both panels (*c*) and (*d*), $Fr = 39$, $Bo = 30$ and $We = Fr\,Bo = 1170$ ($R_0 = 15$ mm, $U_0 = 2.38\ \mathrm{m\,s^{-1}}$). The time stamps shown in panel (*d*) apply to panel (*c*) as well.

2. Experimental set-up and procedure

The experimental set-up consisted of a cylindrical rotating water tank and an electromagnetic dropper (see schematic in figure 1*a*). The spheres were allowed to fall vertically into the water tank from a predetermined height to achieve the desired impact velocity. The sphere release was conducted using an electromagnet dropper. The contact point aligned with the vertical line passing through the sphere's centre of mass, which minimized rotation of the sphere during the release. The cylindrical container made of Plexiglas (diameter $D = 150$ mm, wall thickness $h = 5$ mm) was driven by a motor with a constant angular velocity, $0\ \mathrm{rad\,s^{-1}} \leqslant \omega \leqslant 8\pi\ \mathrm{rad\,s^{-1}}$, about the central, vertical axis. The water impact projectile was a stainless-steel sphere with radius R_0 that varied from 5 mm to 15 mm. The surface of the sphere was coated with a hydrophobic coating, which provided a static contact angle of $\theta = 145 \pm 5^{\circ}$. The steel sphere was released from a height H_0 using the electromagnetic dropper, and impacted the lowest point of the parabolic free surface at an impact velocity $U_0 \approx \sqrt{2gH_0}$, where g is the gravitational acceleration. The true impact velocity is calculated through an analysis using high-speed imaging, and ranges from $0.9\ \mathrm{m\,s^{-1}}$ to $3.2\ \mathrm{m\,s^{-1}}$. The corresponding Reynolds number is $Re \equiv U_0R_0/\nu \sim O(10^4)$, where ν is the kinematic viscosity of water. The air pressure above the pool was atmospheric. Images were recorded using a high-speed camera (Photron Mini AX100) at speeds up to 10^4 frames per second. For the optical configuration used here, image distortion in the vertical direction can be neglected. A ray-tracing model, in conjunction with a grid-based calibration method, was employed to correct for the optical distortion in the horizontal direction.

When the liquid viscosity is low, two independent parameters may be conveniently chosen to fully define the sphere impact problem (Oguz & Prosperetti 1990). Here, we use the Froude and Bond numbers, defined as $Fr \equiv U_0^2/(gR_0)$ and $Bo \equiv \rho g R_0^2/\sigma$, respectively, where ρ is the density of water and σ the surface tension of the air–water interface. In addition, we introduce a dimensionless rotational parameter $\mathcal{S} \equiv \omega R_0/U_0$, which is equivalent to the inverse Rossby number (Warn *et al.* 1995). The Weber number $We \equiv \rho U_0^2 R_0/\sigma$ will also be listed; however, since We can be expressed as the product of Fr and Bo, $We = Fr\,Bo$, it does not serve as an additional control parameter in the present work. A representative snapshot of the underwater cavity that forms after the sphere impacts the rotating pool is shown in figure 1(*b*). A splash crown is visible above the free surface. Below the surface, the sphere has entrained an attached air cavity that pinches off at a later instant, due to the competing effects of inertial, hydrostatic and centripetal forces.

3. Numerical method

In addition to the experiments, we performed boundary integral (BI) simulations based on potential flow theory (Oguz & Prosperetti 1993; Peters *et al.* 2016; Li *et al.* 2020) to better and quantitatively understand the experimental observations. Considering the rotating flow background, we defined a cylindrical coordinate system $Or\theta z$, which was fixed to the rotating cylindrical tank. The origin O was set at the centre of the free surface, and the z axis direction pointed opposite to that of g. The BI can be reduced to two-dimensional simulations here, under the assumption of axisymmetry of the developing cavity. Since a non-inertial coordinate system was adopted, the centrifugal force must be taken into consideration.

The Coriolis force can be neglected in the simulations, as it acts normal to the rz plane and is also of low magnitude when compared to the inertial forces. Additionally, the BI formulation allowed for the inclusion of air as a second ideal fluid phase. The simulations were first validated against quiescent liquid cases: then rotating liquid simulations were performed. Although the BI simulations enable us to accurately model the mechanisms governing the subsurface cavity evolution, they can only serve as a qualitative model for the splash closure.

4. Results and discussion

4.1. *Regime transition of cavity type*

To investigate the effect of the rotating liquid background on the transient cavity dynamics, we compare the experimental results in the quiescent liquid condition to those of the rotating background, at different values of $\mathcal{S}$ while maintaining Fr and Bo constant (see figure 1*c*,*d*). A typical water entry sequence in quiescent liquid is shown in figure 1(*c*), where $Fr = 39$ and $Bo = 30$, and consequently $We = Fr\,Bo = 1170$. Note that the effect of rotation becomes more dramatic with increasing sphere radius R_0, which will be discussed later in § 4.2. The initial impact creates a splash and cavity. A crown-like splash curtain forms above the water surface, which remains open during the entire sequence. The underwater cavity that is created is first pushed out by the descending sphere. Later, it contracts due to the hydrostatic pressure, leading to a pinch-off at $t = 77.0$ ms. This type of pinch-off was referred to as a 'deep seal' in prior work, as it occurs at a significant depth below the water surface when compared to other cavity-sealing phenomena (Lohse *et al.* 2004; Aristoff & Bush 2009; Tan & Thomas 2018). The corresponding cavity is referred to as a deep seal cavity. Note that the pinch-off depth is about half the height of the whole cavity, which is in agreement with prior studies (Oguz & Prosperetti 1990; Duclaux *et al.* 2007; Aristoff & Bush 2009; Bergmann *et al.* 2009*b*).

In comparison, for the rotating liquid case, a splash curtain is faintly observable above the free surface ($t = 12.8$ ms in figure 1*d*). However, the diameter of this splash is significantly lower than that in the quiescent liquid case. By $t = 25.6$ ms, we find that the splash curtain has already closed. This process is commonly referred to as 'surface seal', since the splash crown is pulled radially inwards before finally closing above the free surface (Aristoff & Bush 2009; Truscott *et al.* 2014). We note that, for the quiescent liquid case, a surface seal type of cavity cannot be expected until a high Fr, the threshold for which was estimated as $Fr_c = (1/6400)(\rho/\rho_a)^2 \approx 100$ (Birkhoff & Isaacs 1951), where ρ_a is the density of air. Thus, the presence of a rotating background flow triggers an early transition from the deep seal to the surface seal type of cavity. Once the surface seal has been triggered, the events that succeed are markedly different (Marston *et al.* 2016). The enclosed cavity in the rotating liquid case first undergoes a reduction in pressure due to its expanding volume (from $t = 25.6$ ms to $t = 38.4$ ms). This pressure reduction causes the cavity to be pulled below the free surface, which is often followed by the formation of a Rayleigh–Taylor fingering instability at the apex of the enclosed cavity (see also Aristoff & Bush 2009).

We vary Fr and $\mathcal{S}$ systematically over a wide range ($100 \leq Fr \leq 205$ and $0 \leq \mathcal{S} \leq 0.047$) and characterize the splash and transient cavity dynamics at a fixed $Bo = 3.4$. A phase diagram indicating the dependence of the observed cavity type on Fr and $\mathcal{S}$ is presented in figure 2(*a*). At a relatively low Fr and low $\mathcal{S}$, we observe the deep seal. With increasing $\mathcal{S}$, the cavity closure undergoes a transition from deep seal to surface seal. The transitional Fr decreases ever more steeply with increasing background rotation, until, for $\mathcal{S} \geq 0.045$, we always observe the surface seal cavity type. It is verified that the transitional Fr in the quiescent liquid condition ($\mathcal{S} = 0$) is comparable to the threshold proposed by Birkhoff & Isaacs (1951). Note that the data in figure 2(*a*) are obtained only for $Bo = 3.4$; a change in Bo alters the transitional boundary of the Fr–$\mathcal{S}$ phase space presented here. Mapping out the full non-dimensional Fr–$\mathcal{S}$–Bo parameter space would require even more extensive sets of experiments, which are beyond the scope of the present work. Next, we resort to the BI simulations to obtain the cavity shapes for different values of $\mathcal{S}$. Figure 2(*b*) shows the cavity profiles, in this case without the airflow modelled. With increasing $\mathcal{S}$ the cavity neck becomes narrower, thereby aiding in the transition to the surface seal regime. Yet, remarkably, the effects of rotation seem localized to near the free surface, and the cavity profiles nicely overlap for larger depths inside the pool.

4.2. *Rayleigh–Plesset approach*

To better understand the experimental results, we adapt the Rayleigh–Plesset equation (Plesset & Prosperetti 1977) for an axisymmetrically evolving cavity in cylindrical coordinates (r, θ, z) (Oguz & Prosperetti 1990; Lohse *et al.* 2004; Bergmann *et al.* 2009*a*; Lohse 2018). Based on the BI simulation results, the axial velocity U_z can be neglected in comparison to the radial U_r and azimuthal U_θ components. Applying the continuity equation, we then obtain $rU_r = R\dot{R}$, where R denotes the radius of the cavity wall. Integrating the Rayleigh–Plesset equation radially with respect to r from R to R_∞, we obtain

$$\frac{\mathrm{d}(R\dot{R})}{\mathrm{d}t} \ln \frac{R}{R_\infty} + \frac{1}{2}\dot{R}^2 \left(1 - \frac{R^2}{R_\infty^2}\right) = \frac{2\nu\dot{R}}{R} + \frac{\sigma}{\rho R} + \frac{P_\infty - P}{\rho} - \int_R^{R_\infty} \frac{U_\theta^2}{r}\,\mathrm{d}r, \tag{4.1}$$

where P_∞ is the pressure (in water) at a distance R_∞, at which the flow may be regarded as quiescent, and P the air pressure inside the cavity. In the high-Reynolds-number and high-Weber-number limit of our experiments, the first and second terms on the right-hand side of (4.1) can be safely ignored. Finally, we assume that the azimuthal velocity in the

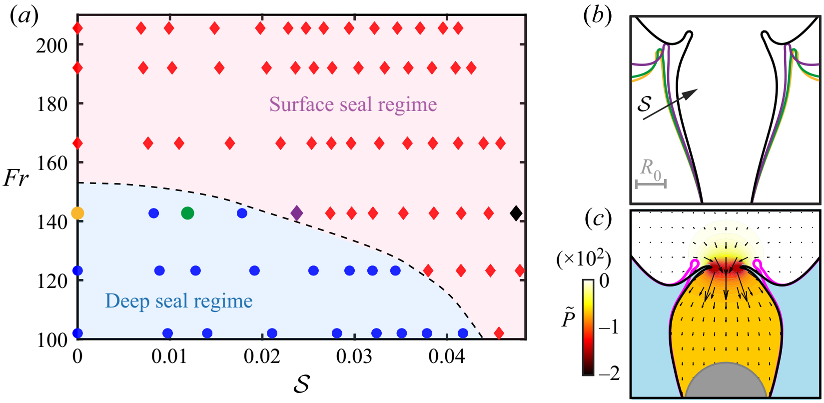

Figure 2. (*a*) Phase diagram showing the observed cavity types in experiments and their dependence on Fr and $\mathcal{S}$ for $Bo = 3.4$. The red diamonds and blue circles denote experiments with observed surface seal and deep seal, respectively. For $Fr < 167$, the transition in the cavity type can be strongly influenced by tuning $\mathcal{S}$. The four bigger symbols marked with colours refer to the curves with the same colour in (*b*), for which BI simulations were conducted. (*b*) BI simulation results of the cavity shape for various values of $\mathcal{S}$ at $Fr = 143$ and $Bo = 3.4$. The time is $t = 10$ ms after impacting. The yellow, green, purple and black curves denote the cavity formed at $\mathcal{S} = 0$, 0.012, 0.024 and 0.047, respectively. These results were obtained without considering the effect of air. (*c*) BI simulations showing the normalized pressure field $\tilde{P} = (P - P_a)/\left(\frac{1}{2}\rho_a U_0^2\right)$ in air during water entry of a sphere. Here, P_a is the ambient pressure and ρ_a is the density of air. The airflow reduces the pressure near the cavity neck. Here, $Fr = 103$, $Bo = 13.4$ and $\mathcal{S} = 0.079$. The time is $t = 8$ ms after impacting. BI simulations of the closure of the splash curtain are shown with (black curve) and without (magenta curve) the effect of air included.

pool remains unchanged beyond the vicinity of the developing cavity, i.e. $U_\theta \approx \omega R$. These approximations lead to

$$\frac{\mathrm{d}(\tilde{R}\dot{\tilde{R}})}{\mathrm{d}\tilde{t}} \ln \frac{\tilde{R}}{\tilde{R}_\infty} + \frac{1}{2}\dot{\tilde{R}}^2\left(1 - \frac{\tilde{R}^2}{\tilde{R}_\infty^2}\right) = -\frac{\tilde{z}}{Fr} + \frac{1}{2}\mathcal{S}^2\tilde{R}^2, \tag{4.2}$$

where the characteristic length and time scales used in this non-dimensional representation are R_0 and R_0/U_0, respectively. On the right-hand side, the dimensionless rotational number $\mathcal{S}$ appears as an additional pressure term, which speeds up the closure of the cavity.

In light of (4.2), one can rationalize the cavity behaviours that were observed experimentally. Firstly, we note that both the hydrostatic term $-\tilde{z}/Fr$ and the rotational term $(\mathcal{S}^2\tilde{R}^2)/2$ contribute to speeding up the cavity collapse. The latter is unchanged with depth, and (assuming $R \sim R_0$) is of relevance only up to a shallow depth estimated as $z \leq (\omega^2 R_0^2/g)/2$. For the most extreme rotation rate in experiments, i.e. $\mathcal{S} = 0.04$ at $Bo = 3.4$, this yields a region of influence $z \sim R_0$. Beyond this depth below the free surface, the dynamics is dominated by the hydrostatic term. Thus, the rotating liquid seems to influence the cavity profiles only up to a shallow depth, a result that is also corroborated by our BI simulations (figure 2*b*).

Further to the increased pressure term $(\mathcal{S}^2\tilde{R}^2)/2$ in (4.2), the airflow through the narrowing splash curtain also contributes to the early surface seal in the rotating liquid case. We turn our focus to the splash radius $R_{sp}(t)$ near the free surface. Here the hydrostatic term can be safely neglected, but, instead, the Bernoulli pressure reduction due to air entering the cavity becomes important. The volume expansion rate of the cavity can be expressed as $\dot{\mathcal{V}} = \mathrm{d}(\int \pi R^2 \,\mathrm{d}z)/\mathrm{d}t$. Since it is known that the role of rotation is localized to near the free surface (see figure 2*b*), we can assume that $\dot{\mathcal{V}}$ is unchanged with $\mathcal{S}$. Therefore, the continuity constraint necessitates that the mean airflow velocity near the free surface $U_{za} \propto 1/R_{sp}^2$. The corresponding under-pressure is $\Delta P \propto (\rho_a R_{sp}^{-4})/2$, which indicates that even a slight reduction in the splash radius can induce a cascading effect due to the inherent aerodynamic coupling, leading to the early surface seal. The surface seal time (defined as the time interval between the impacting moment and the surface seal moment) decreases with increasing $\mathcal{S}$. However, the precise moment of surface seal is difficult to estimate from side-view images in the rotating liquid cases. It would require additional recordings from above the free surface, which will be part of a future investigation. The role of the incoming air is further exemplified in the BI simulations of the pressure field in the air at an instant prior to the surface closure (see figure 2*c*). The pressure in the narrow neck region is significantly lower than that in the surrounding regions. In contrast, a simulation that ignores the airflow effect gives a noticeably wider opening near the free surface (magenta curve).

4.3. *Underwater pinch-off of cavity*

While the background liquid rotation triggers an earlier transition from a deep seal to a surface seal, there exists a range of Froude numbers for which the transition is not triggered (see deep seal regime in figure 2*a*). However, even within the deep seal regime, the rotation induces changes to the underwater cavity dynamics. Since the effect of background liquid rotation on cavity dynamics is more pronounced for the larger R_0 cases, as discussed in § 4.2, we used larger spheres ($Bo = 13.4$ and 30) to study the underwater cavity dynamics in the deep seal regime. These Bo values, although larger than the $Bo = 3.4$ in figure 2(*a*), help demonstrate the dramatic effect of background liquid rotation on the subsurface cavity dynamics. We define the pinch-off time t_p as the time interval between the moment the sphere touches the initial air–water interface and the moment of the cavity collapse. In figure 3(*a*), we plot the non-dimensional pinch-off time $t_p^* = t_p U_0/R_0$ as a function of $Fr^{1/2}$, with ω varied from 0 rad s^{-1} to 8π rad s^{-1}. Prior studies (Glasheen & McMahon 1996; Duclaux *et al.* 2007; Truscott & Techet 2009*b*) have shown that the non-dimensional pinch-off time follows a square-root relation $t_p^* = k_t Fr^{1/2}$, where k_t is a constant. As evident from figure 3(*a*), the scaling $t_p^* = k_t Fr^{1/2}$ is robust for the rotating flow cases as well. The prefactor k_t ranges from 1.63 to 2.09, which is comparable to the value reported in prior work (≈1.726; Truscott & Techet 2009*b*). However, the prefactor k_t decreases noticeably with increase in ω (see inset to figure 3*a*). Beyond the Fr range of 5.6–35 presented here, since the cavity undergoes surface seal, the deep seal time definition is somewhat ambiguous and hence will not be reported.

Lastly, we reveal the dynamics of the cavity wall at the pinch-off depth as it accelerates towards the singularity of the pinch-off. Close enough to the pinch-off point, the cavity radius R is small, while the reference radius R_∞ is very large. Therefore, the logarithmic part of the inertial term in (4.2), i.e. $\ln(\tilde{R}/\tilde{R}_\infty)$, diverges. This necessitates the condition that $\mathrm{d}(\tilde{R}\dot{\tilde{R}})/\mathrm{d}\tilde{t} = 0$. Integrating this, we obtain $R = k_R\sqrt{R_0U_0}\,\tau^{1/2}$, where $\tau = (t_p - t)$ denotes the time to pinch-off. In figure 3(*b*), we plot R/R_0 as a function of $(\tau U_0/R_0)^{1/2}$ for various values of $\mathcal{S}$. The data collapse nicely with a good agreement to the 1/2 power-law prediction. The prefactor of the fit remains nearly constant ($k_R = 0.28 \pm 0.01$) across the cases. When we focus on the final stage of the collapse ($(\tau U_0/R_0)^{1/2} < 2$), the direct fitting between R/R_0 and $\tau U_0/R_0$ gives a power-law exponent of approximately 0.54 for all $\mathcal{S}$ cases, which is close to the value recently found in experiments (0.55; Yang,

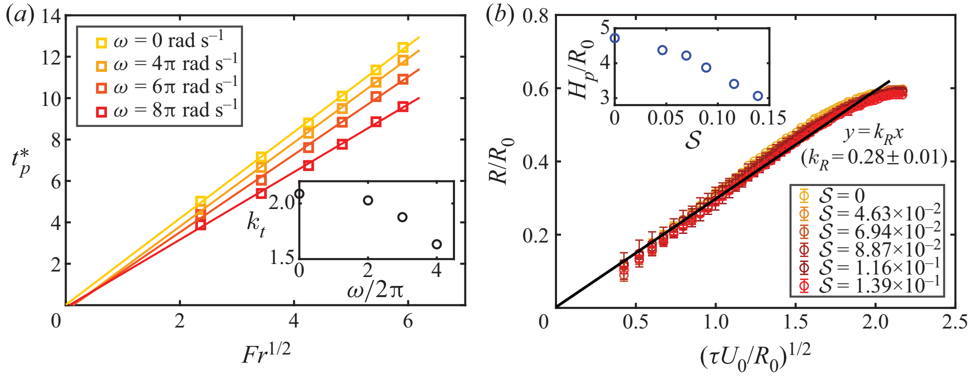

Figure 3. (*a*) Non-dimensional pinch-off time t_p^* as a function of $Fr^{1/2}$ for various values of $\omega = 0$ rad s^{-1}, 4π rad s^{-1}, 6π rad s^{-1} and 8π rad s^{-1} for $Bo = 30$. The lines represent best fits to the experimental datasets. The inset shows the prefactor k_t, obtained using least-squares fitting, for different values of $\omega/(2\pi)$. (*b*) Normalized cavity radius R/R_0 as a function of $(\tau U_0/R_0)^{1/2}$ for datasets with different $\mathcal{S}$. Here, τ is the time to pinch-off. The inset shows the normalized pinch-off depth H_p/R_0 as a function of $\mathcal{S}$. Here, $Fr = 33$, $Bo = 13.4$ and $We = Fr\,Bo = 449$.

Tian & Thoroddsen 2020). This is also consistent with previous experiments (Bergmann *et al.* 2006) and the corresponding slow asymptotic theory (Eggers *et al.* 2007). Therefore, the effect of the background liquid rotation is insignificant during the final stages of the cavity evolution. The inset to figure 3(*b*) shows that the normalized pinch-off depth H_p/R_0 monotonically decreases with increasing $\mathcal{S}$. This trend can again be traced back to the increased pressure in the liquid and the reduced cavity pressure due to the inrushing airflow (see § 4.2).

5. Conclusions

In summary, we have presented a combined experimental, numerical and theoretical investigation of the transient cavity dynamics following the impact of a heavy sphere into a rotating pool of water. Background liquid rotation triggers an early transition from a deep seal to a surface seal regime. We characterized this regime transition in terms of the Froude number Fr and a dimensionless rotational number $\mathcal{S} \equiv \omega R_0/U_0$. With increasing $\mathcal{S}$, the transitional Fr marking the change of the cavity type decreases. The reasons for this can be traced back to the additional pressure term arising due to the background rotation, in combination with the Bernoulli pressure reduction due to the airflow through the splash neck above the free surface. We used BI simulations to demonstrate the crucial role of air on the splash and cavity dynamics. By comparing two simulations modelled with and without air, we show that incoming airflow can dramatically affect the splash closure time. It is revealed that the pressure buildup in the rotating liquid accelerates the closure phenomenon, thereby inducing the early transition from deep seal to surface seal. Below the transitional Fr, we investigated the effect of background rotation on the dynamics of the deep seal cavity. Remarkably, the non-dimensional pinch-off time retains a 1/2 power-law dependence on Fr despite the centripetal effects, but with a noticeably reduced prefactor with increasing ω.

We used the axisymmetric Rayleigh–Plesset equation to predict the radius evolution during the final moments before the pinch-off, which yields a $\tau^{1/2}$ dependence, where

τ is the time to pinch-off. The predictions are found to be in good agreement with the experimental measurements.

The current work has revealed that the effects of a rotating liquid background are mainly confined to the free surface and to shallow depths. Yet, these initial-phase modifications have noticeable effects on the later dynamics of water entry.

Acknowledgements. We thank S. Maheshwari, Q. Zhou and L. Jiang for useful discussions.

Funding. We acknowledge financial support by the Natural Science Foundation of China under grant nos. 11988102, 11861131005, 91852202 and 11672156.

Declaration of interests. The authors report no conflict of interest.

Author ORCIDs.

- Lei Yi https://orcid.org/0000-0002-0247-4600;
- Shuai Li https://orcid.org/0000-0002-3043-5617;
- Hechuan Jiang https://orcid.org/0000-0003-3069-0586;
- Detlef Lohse https://orcid.org/0000-0003-4138-2255;
- Chao Sun https://orcid.org/0000-0002-0930-6343;
- Varghese Mathai https://orcid.org/0000-0001-7296-6056.

REFERENCES

ALVAREZ-LACALLE, E., CASADEMUNT, J. & EGGERS, J. 2009 Pinch-off singularities in rotating Hele-Shaw flows at high viscosity contrast. *Phys. Rev.* E **80**, 056306.

ALY, A.M. & ASAI, M. 2018 Water entry of decelerating spheres simulations using improved ISPH method. *J. Hydrodyn.* **30**, 1120–1133.

ARISTOFF, J.M. & BUSH, J.W.M. 2009 Water entry of small hydrophobic spheres. *J. Fluid Mech.* **619**, 45–78.

ARISTOFF, J.M., TRUSCOTT, T.T., TECHET, A.H. & BUSH, J.W.M. 2010 The water entry of decelerating spheres. *Phys. Fluids* **22**, 032102.

BERGMANN, R., ANDERSEN, A., VAN DER MEER, D. & BOHR, T. 2009*a* Bubble pinch-off in a rotating flow. *Phys. Rev. Lett.* **102**, 204501.

BERGMANN, R., VAN DER MEER, D., GEKLE, S., VAN DER BOS, A. & LOHSE, D. 2009*b* Controlled impact of a disk on a water surface: cavity dynamics. *J. Fluid Mech.* **633**, 381–409.

BERGMANN, R., VAN DER MEER, D., STIJNMAN, M., SANDTKE, M., PROSPERETTI, A. & LOHSE, D. 2006 Giant bubble pinch-off. *Phys. Rev. Lett.* **96**, 154505.

BIRKHOFF, G. & ISAACS, R. 1951 Transient cavities in air–water entry. *Tech. Rep.* Navord Report 1490. United States Naval Ordnance Laboratory.

DUCLAUX, V., CAILLÉ, F., DUEZ, C., YBERT, C., BOCQUET, L. & CLANET, C. 2007 Dynamics of transient cavities. *J. Fluid Mech.* **591**, 1–19.

DUEZ, C., YBERT, C., CLANET, C. & BOCQUET, L. 2007 Making a splash with water repellency. *Nat. Phys.* **3**, 180–183.

EGGERS, J., FONTELOS, M.A., LEPPINEN, D. & SNOEIJER, J.H. 2007 Theory of the collapsing axisymmetric cavity. *Phys. Rev. Lett.* **98**, 094502.

ENRIQUEZ, O.R., PETERS, I.R., GEKLE, S., SCHMIDT, L.E., LOHSE, D. & VAN DER MEER, D. 2012 Collapse and pinch-off of a non-axisymmetric impact-created air cavity in water. *J. Fluid Mech.* **701**, 40–58.

ESHRAGHI, J., JUNG, S. & VLACHOS, P.P. 2020 To seal or not to seal: the closure dynamics of a splash curtain. *Phys. Rev. Fluid* **5**, 104001.

GEKLE, S., VAN DER BOS, A., BERGMANN, R., VAN DER MEER, D. & LOHSE, D. 2008 Noncontinuous Froude number scaling for the closure depth of a cylindrical cavity. *Phys. Rev. Lett.* **100**, 084502.

GLASHEEN, J.W. & MCMAHON, T.A. 1996 Vertical water entry of disks at low froude numbers. *Phys. Fluids* **8**, 2078–2083.

HAO, J., ZHANG, M. & HUANG, X. 2018 The influence of surface roughness on cloud cavitation flow around hydrofoils. *Acta Mechanica Sin.* **34**, 10–21.

HU, D.L. & BUSH, J.W.M. 2010 The hydrodynamics of water-walking arthropods. *J. Fluid Mech.* **644**, 5–33.

Jiang, H., Zhu, X., Wang, D., Huisman, S.G. & Sun, C. 2020 Supergravitational turbulent thermal convection. *Sci. Adv.* **6**, eabb8676.

Li, S., van der Meer, D., Zhang, A.-M., Prosperetti, A. & Lohse, D. 2020 Modelling large scale airgun-bubble dynamics with highly non-spherical features. *Intl J. Multiphase Flow* **122**, 103143.

Lohse, D. 2018 Bubble puzzles: from fundamentals to applications. *Phys. Rev. Fluid* **3**, 110504.

Lohse, D., Bergmann, R., Mikkelsen, R., Zeilstra, C., van der Meer, D., Versluis, M., van der Weele, K., van der Hoef, M. & Kuipers, H. 2004 Impact on soft sand: void collapse and jet formation. *Phys. Rev. Lett.* **93**, 198003.

Mansoor, M.M., Marston, J.O., Vakarelski, I.U. & Thoroddsen, S.T. 2014 Water entry without surface seal: extended cavity formation. *J. Fluid Mech.* **743**, 295–326.

Mansoor, M.M., Vakarelski, I.U., Marston, J.O., Truscott, T.T. & Thoroddsen, S.T. 2017 Stable-streamlined and helical cavities following the impact of Leidenfrost spheres. *J. Fluid Mech.* **823**, 716–754.

Marston, J.O., Truscott, T.T., Speirs, N.B., Mansoor, M.M. & Thoroddsen, S.T. 2016 Crown sealing and buckling instability during water entry of spheres. *J. Fluid Mech.* **794**, 506–529.

Mathai, V., Govardhan, R.N. & Arakeri, V.H. 2015 On the impact of a concave nosed axisymmetric body on a free surface. *Appl. Phys. Lett.* **106**, 064101.

Mathai, V., Lohse, D. & Sun, C. 2020 Bubbly and buoyant particle-laden turbulent flows. *Annu. Rev. Condens. Matter Phys.* **11**, 529–559.

Oguz, H.N. & Prosperetti, A. 1990 Bubble entrainment by the impact of drops on liquid surfaces. *J. Fluid Mech.* **219**, 143–179.

Oguz, H.N. & Prosperetti, A. 1993 Dynamics of bubble growth and detachment from a needle. *J. Fluid Mech.* **257**, 111–145.

Peters, I.R., Madonia, M., Lohse, D. & van der Meer, D. 2016 Volume entrained in the wake of a disk intruding into an oil-water interface. *Phys. Rev. Fluids* **1**, 033901.

Plesset, M.S. & Prosperetti, A. 1977 Bubble dynamics and cavitation. *Annu. Rev. Fluid Mech.* **9**, 145–185.

Prosperetti, A. & Oguz, H.N. 1993 The impact of drops on liquid surfaces and the underwater noise of rain. *Annu. Rev. Fluid Mech.* **25**, 577–602.

Shi, H.-H., Itoh, M. & Takami, T. 2000 Optical observation of the supercavitation induced by high-speed water entry. *Trans. ASME: J. Fluids Engng* **122**, 806–810.

Stepanyants, Y.A. & Yeoh, G.H. 2008 Stationary bathtub vortices and a critical regime of liquid discharge. *J. Fluid Mech.* **604**, 77–98.

Tan, B.C.-W. & Thomas, P.J. 2018 Influence of an upper layer liquid on the phenomena and cavity formation associated with the entry of solid spheres into a stratified two-layer system of immiscible liquids. *Phys. Fluids* **30**, 064104.

Thoroddsen, S.T., Etoh, T.G., Takehara, K. & Takano, Y. 2004 Impact jetting by a solid sphere. *J. Fluid Mech.* **499**, 139–148.

Thoroddsen, S.T., Thoraval, M.-J., Takehara, K. & Etoh, T.G. 2011 Droplet splashing by a slingshot mechanism. *Phys. Rev. Lett.* **106**, 034501.

Truscott, T.T., Epps, B.P. & Belden, J. 2014 Water entry of projectiles. *Annu. Rev. Fluid Mech.* **46**, 355–378.

Truscott, T.T. & Techet, A.H. 2009*a* A spin on cavity formation during water entry of hydrophobic and hydrophilic spheres. *Phys. Fluids* **21**, 121703.

Truscott, T.T. & Techet, A.H. 2009*b* Water entry of spinning spheres. *J. Fluid Mech.* **625**, 135–165.

Vakarelski, I.U., Klaseboer, E., Jetly, A., Mansoor, M.M., Aguirre-Pablo, A.A., Chan, D.Y.C. & Thoroddsen, S.T. 2017 Self-determined shapes and velocities of giant near-zero drag gas cavities. *Sci. Adv.* **3**, e1701558.

Van Der Meer, D. 2017 Impact on granular beds. *Annu. Rev. Fluid Mech.* **49**, 463–484.

Vincent, L., Xiao, T., Yohann, D., Jung, S. & Kanso, E. 2018 Dynamics of water entry. *J. Fluid Mech.* **846**, 508–535.

Warn, T., Bokhove, O., Shepherd, T.G. & Vallis, G.K. 1995 Rossby number expansions, slaving principles, and balance dynamics. *Q. J. R. Meteorol. Soc.* **121**, 723–739.

Yang, Z.Q., Tian, Y.S. & Thoroddsen, S.T. 2020 Multitude of dimple shapes can produce singular jets during the collapse of immiscible drop-impact craters. *J. Fluid Mech.* **904**, A19.

Zhang, X., Liu, P.-Q., Qu, Q.-L., Wang, R. & Agarwal, R.K. 2018 Effects of Froude number and geometry on water entry of a 2-D ellipse. *J. Hydrodyn.* **30**, 738–749.